

©2018. American Geophysical Union. All Rights Reserved. Access to this work was provided by the University of Maryland, Baltimore County (UMBC) ScholarWorks@UMBC digital repository on the Maryland Shared Open Access (MD-SOAR) platform.

Please provide feedback

Please support the ScholarWorks@UMBC repository by emailing scholarworks-group@umbc.edu and telling us what having access to this work means to you and why it's important to you. Thank you.

JGR Atmospheres

RESEARCH ARTICLE

10.1029/2019JD030658

Key Points:

- Doppler lidar wind profile analysis at three fixed observation sites for 30 southerly low-level jets, plus 11 cold-frontal northerly jets
- Stronger low-level jets are preceded by deeper convective mixed layers and stronger boundary layer wind speeds
- Stronger southerly jets are associated with a larger number of pristine convection initiation events per night

Supporting Information:

- Supporting Information S1

Correspondence to:

B. J. Carroll,
brian.carroll@umbc.edu

Citation:

Carroll, B. J., Demoz, B. B., & Delgado, R. (2019). An overview of low-level jet winds and corresponding mixed layer depths during PECAN. *Journal of Geophysical Research: Atmospheres*, 124, 9141–9160. <https://doi.org/10.1029/2019JD030658>

Received 18 MAR 2019

Accepted 26 JUL 2019

Accepted article online 9 AUG 2019

Published online 23 AUG 2019

An Overview of Low-Level Jet Winds and Corresponding Mixed Layer Depths During PECAN

Brian J. Carroll^{1,2} , Belay B. Demoz^{1,2} , and Ruben Delgado^{1,2} 

¹Department of Physics, University of Maryland, Baltimore County, Baltimore, MD, USA, ²Joint Center for Earth Systems Technology, University of Maryland, Baltimore County, Baltimore, MD, USA

Abstract Thirty southerly low-level jet (LLJ) events were observed during the Plains Elevated Convection at Night (PECAN) field campaign in the Great Plains region of the United States during summer 2015. Here we present Doppler lidar wind data from three PECAN instrumentation sites to explore characteristics of LLJs and the boundary layer as well as some of the heterogeneities possible within the wind field of a LLJ. Southerly LLJs were observed on 66% of nights at the southwestern site (Greensburg, KS) but only 56% and 53% of nights at the eastern and northern sites, respectively (Hesston and Ellis, KS). The northernmost site had a relative abundance of weaker jets or nonjet conditions due to fronts or convective systems that only affected part of the observation domain. Plotting mean wind fields of each LLJ type reveals that the strongest LLJs tend to develop under very similar conditions but begin to show variability in wind profile evolution after several hours. A robust mixed layer height retrieval algorithm is used to investigate the interplay between the jets and the turbulent convective boundary layer, showing that stronger LLJs are preceded by deeper afternoon mixed layers and often have a later decoupling of mixing between the upper convective mixed layer and the near-surface layer. Only the strongest LLJs generated a shallow mixing layer overnight. Comparing jet strength and direction to pristine nocturnal convection initiation shows that the strongest southerly LLJs yielded the most pristine nocturnal convection initiation events per night, and the pristine nocturnal convection initiation occurred farther north.

1. Introduction

The low-level jet (LLJ) is defined as a wind speed maximum within the lower troposphere with a large decrease in wind speed above the maximum (Bonner, 1968; Shapiro et al., 2016; Song et al., 2005; Whiteman et al., 1997). LLJs are found in many locations around the world with a variety of forcing mechanisms and impacts (Higgins et al., 1997; Rife et al., 2010; Stensrud, 1996). The most studied LLJ is that of the Great Plains region of the United States due to its high frequency of occurrence and strong wind speeds spanning hundreds of kilometers along-track and cross-track. The frequency, strength, and location of the Great Plains LLJ allow it to play a significant role in regional weather; it is a source of wind field convergence and the southerly LLJs typically carry warm and moist air northward to fuel convective systems (Barandiaran et al., 2013; Gebauer et al., 2018; Helfand & Schubert, 1995; Higgins et al., 1997; Houze, 2004; Stelten & Gallus, 2017; Wu & Raman, 1998). LLJs are also important for air quality, capable of transporting atmospheric constituents hundreds of kilometers and in some cases are associated with high concentrations at the surface (Banta et al., 1998; Delgado et al., 2015; Klein et al., 2014; Mao & Talbot, 2004). The LLJ over land is primarily a nocturnal phenomenon, with wind speeds ramping up around sunset and dying down with the rise of the morning convective boundary layer. The wind speed maximum is typically below 500 m above ground level (AGL). These impacts and properties primarily refer to the common southerly LLJ, but similar wind speed profiles are also observed with a northerly direction over the Great Plains. These northerly jets (NJs) are typically found behind cold fronts and have different forcing mechanisms and impacts than LLJs, generally featuring smaller wind speed maxima and much less promotion of precipitation (Doubler et al., 2015; Song et al., 2005; Walters et al., 2008; Walters et al., 2014; Whiteman et al., 1997). In this study, NJs are addressed as a separate phenomenon.

The mechanisms governing LLJ wind fields are still in debate despite having been discussed in the literature for over 60 years. Consensus has settled on inertial oscillation (IO) theory (initially proposed by Blackadar (1957)) as the dominant driver of the common southerly LLJ, but IO alone cannot reproduce all observed LLJs. Baroclinicity induced by diurnal heating of sloped terrain (introduced by Holton

(1967)) is also cited as a vital forcing mechanism and has been combined with IO theory to produce diurnal LLJ wind field models that are in good agreement with observations (Du & Rotunno, 2014; Fedorovich et al., 2017; Shapiro et al., 2016). NJs cannot be accurately modeled with only those two key mechanisms of LLJs. Ostdiek and Blumen (1997) studied an NJ caused by deformation frontogenesis with associated IO. More recently, Gebauer et al. (2017) performed a theoretical analysis of NJs with a one-dimensional analytical model. They concluded that the strong capping inversion commonly found with cold air outbreaks can reduce surface buoyancy and enhance northerly geostrophic wind, and thus, cold intrusions (e.g., fronts) are likely a key factor in creating NJs over the slope of the Great Plains. Overall, NJs have been studied far less in the literature than LLJs from both observational and modeling standpoints.

Climatological studies using rawinsonde data (e.g., Bonner, 1968; Walters et al., 2008; Whiteman et al., 1997), radar profiler data (Arritt et al., 1997), or reanalysis data (e.g., Anderson & Arritt, 2001; Berg et al., 2015; Doubler et al., 2015; Walters et al., 2014) have formed the basis for expected LLJ behavior and explore interannual variability. These studies are well-suited for determining seasonal or monthly geographic preference and strength of LLJs, highlighting the warm season strong southerly nocturnal LLJ. A major limitation of rawinsonde-based studies is sparse sampling, typically limited to twice-daily soundings (0000 UTC and 1200 UTC). Little information can be gathered about the evolution of the wind field for a given event, and sampling may be biased toward long-lived synoptically driven cases (Walters et al., 2008). Climatologies based on reanalysis data improve upon the rawinsonde temporal sampling limitation and provide better spatial resolution than rawinsonde stations, but may still have inaccuracies. Walters et al. (2014) compared the North American Regional Reanalysis (NARR) with rawinsonde observations, finding NARR LLJ frequency to be significantly smaller than that from rawinsondes, and a failure to concurrently identify LLJs in rawinsondes and NARR in over 40% of LLJ observations. They concluded that NARR is valuable for LLJ climatological studies but should be used cautiously for case studies or other shorter-term investigations, and that these strengths and weaknesses likely extend to other reanalysis data sets.

Beyond climatologies, three-dimensional evolution of the LLJ wind field has been resolved in finer resolution through case studies drawing from field campaign data sets and more permanent installations, including CASES-99 (1999, southeastern Kansas; R. M. Banta et al., 2002), ABLE (1997–2002, southeastern Kansas; Song et al., 2005), JU2003 (2003, Oklahoma; Hu et al., 2013; P. M. Klein et al., 2016; Lundquist & Mirocha, 2008; Wang et al., 2007), LABLE-I (2012, Oklahoma; Bonin et al., 2015; P. Klein et al., 2015), and CWEX (2013, Iowa; Vanderwende et al., 2015). These studies utilized a variety of in situ and remote sensing instrumentation to investigate details of LLJ wind profile evolution and ties to their environment such as decreasing stability in the boundary layer. Except for ABLE (and CASES-99, which used the ABLE network), these past campaigns only had continuous wind profiling at a single site. The Plains Elevated Convection at Night (PECAN) field campaign of 1 June to 15 July 2015 provides an expansive modern data set to explore these topics, with multiple fixed and mobile instrument sites spread throughout the central Great Plains (Geerts et al., 2017).

PECAN LLJ data have thus far been used for discussion of dynamic forcing mechanisms and for investigating the LLJ's role in convective initiation (CI). Parish (2016) details the environment and forcing of the strong 3 June LLJ using aircraft data and the North American Mesoscale Model, commenting on the relative importance of IO for driving the chosen event over the climatological significance of sloped terrain theory. Parish and Clark (2017) reach similar conclusions for the 20 June LLJ using the North American Mesoscale Model, aircraft, the Weather Research and Forecasting model, and soundings from one ground site. Fedorovich et al. (2017) used numerical modeling and sounding profiles to discuss LLJ impacts on turbulence and advection of environmental potential temperature and how these feed back to affect LLJ structure, also showing that weak LLJs can form on the sloped terrain of the Great Plains in the absence of the geostrophic wind that is fundamental to IO theory. PECAN data have also been used to investigate LLJ influence on nocturnal CI, both related to surface fronts (Trier et al., 2017) and more pristine environments (Gebauer et al., 2018; Shapiro et al., 2018). Hitchcock et al. (2019) performed an in-depth study of all PECAN mesoscale convective system (MCS) environments, highlighting the LLJ's contribution to MCS development. Groundbreaking findings on the importance of spatial and temporal heterogeneities in LLJ evolution have been explored in Gebauer et al. (2018) and Smith et al. (2019), who each examined three strong LLJ

events and found that buoyancy gradients across the slope of the Great Plains can produce local maxima in the wind speed profile that descend over time at a fixed site. These wind features, called “diagonal striations,” are indicative of the LLJ strengthening earlier in the west, enhancing wind at higher altitudes to the east as the westerly component grows. This elevated advection and convergence of the westerly component can generate CI in north-south line structures (Gebauer et al., 2018). While this heterogeneity is important to forecasting CI, the diagonal striations are not found in all LLJs (Smith et al., 2019).

In this study we provide a full-campaign overview of the boundary layer winds at three PECAN instrumentation sites (fixed PECAN integrated sounding arrays, or FPs), exploring similarities and differences among the nightly jet events and between sites. The LLJ is a mesoscale phenomenon covering larger areas than this three-site domain and persisting for several hours, and yet this three-site approach reveals a variety of heterogeneities possible within the wind field of any given LLJ as well as distinct patterns in jet characteristics at each site. The 47-day time span of observations is short enough for a detailed time series analysis but the period also includes multiple synoptic environment changes and frontal passages. We analyze all 30 LLJ events that occurred during PECAN, plus comparison to nights without jets and to NJ events. Directional (LLJ or NJ) and speed categorization is used to show that stronger southerly jets are associated with an increase in pristine nocturnal CI (PNCI) events. Despite the prevalence of LLJs throughout the campaign, only seven nightly intensive observation periods were devoted to LLJ observations and no prior publication has addressed the LLJ in detail with a full-campaign perspective. Although PECAN mobile site observations are not incorporated here due to their discontinuous data sets, some future investigations could benefit from the extensive mobile measurements, especially on LLJ intensive observation period nights.

The primary tool used in this study is Doppler lidar, which is well-suited for providing boundary layer wind profiles with sufficient vertical and temporal resolution to resolve jet features in detail. In addition to wind profiles, a novel algorithm for retrieving mixed layer height (MLH) from Doppler lidar developed by Bonin et al. (2018) is used at one site to explore MLHs preceding LLJs of different strengths. While properties of the daytime convective boundary layer (CBL) and evening transition are known to have important connections to LLJ properties and development, especially for IO theory (e.g., Klein et al., 2016), to the authors' knowledge no past study has examined MLH or CBL height in relation to LLJs. These MLHs also provide a new perspective on understanding nocturnal turbulence associated with LLJs, which in previous studies has often been limited to surface or tower observations despite recognition that near-surface parameters cannot fully represent the LLJ (Banta et al., 2003; Banta et al., 2006; Bonin et al., 2015; Ohya et al., 2008; Sun et al., 2012). This turbulent mixing is important to environmental stability and feedback on LLJ structure.

The next section of this paper (section 2) discusses relevant context of the PECAN field project and details on the Doppler lidars used for this study. Methodology for classifying jet strength is also presented. Section 3 provides an in-depth analysis of the jet events observed during PECAN, focusing on wind profile evolution and MLH behavior. In section 4 the jets' association with PNCI is shown. Summary and discussion are in section 5, along with directions for future research.

2. Instrumentation and Analysis Procedures

The PECAN field campaign spanned 1 June to 15 July of 2015 (Geerts et al., 2017). PECAN featured intensive observations with the goal of improving understanding and forecasting of Great Plains nocturnal convection and related events, including a focus on LLJs. The PECAN domain encompassed most of Kansas and parts of surrounding states as shown in Figure 1, and a southern portion of the domain overlaps with the climatological maximum of LLJ occurrence frequency, which is the area where strong LLJs are most common during the warm season (Bonner, 1968; Doubler et al., 2015). Six FPs were spread throughout the domain.

The observations utilized in this study come from the instrumentation sites FP2, FP3, and FP6 which were in the Kansas cities of Greensburg, Ellis, and Hesston, respectively. The separation between any two sites ranges from 150 to 205 km with longitudinal and latitudinal variation, appropriate for studying mesoscale features of the synoptically driven LLJ. We present data from Doppler lidars at the three chosen sites, along with rawinsonde profiles used as quality assurance for the lidar wind retrievals.

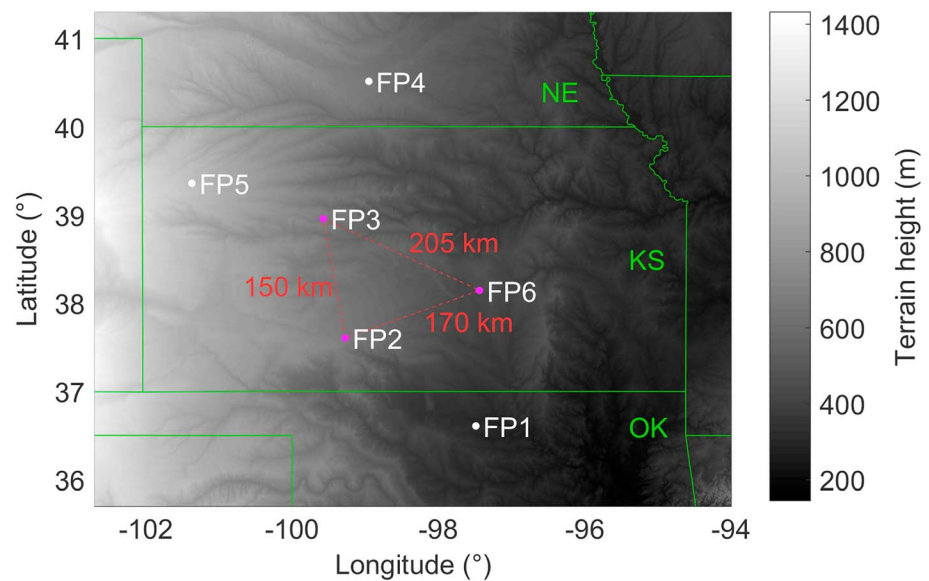


Figure 1. PECAN domain schematic. FPs are fixed integrated sounding arrays. Those marked in magenta (FP2, FP3, and FP6) are used in this study, with separation distances noted in red.

FP1 is omitted from this study because the Doppler lidar installed at that site had a relatively short maximum range (this range is variable based on atmospheric conditions; e.g., aerosol loading) that was often unable to observe the full jet profile shape. This prevents accurate automated detection of jet characteristics. FP4 and FP5 are omitted from this study because they did not host Doppler lidars.

2.1. Doppler Lidar

FP2, FP3, and FP6 each hosted a Doppler lidar that provided boundary layer wind profiles, and in some cases additional information such as the MLH retrieval at FP2 (Delgado et al., 2016; Hanesiak & Turner, 2016a; Hanesiak & Turner, 2016b). Relevant details on each lidar are given in Table 1. FP3 used the Doppler beam swinging (DBS) technique to retrieve profiles of the horizontal wind vector, whereas FP2 and FP6 used conical Planned Position Indicator (PPI) scans and the velocity azimuth display (VAD) technique for wind retrieval. The standard VAD technique using a single PPI was first introduced by Browning and Wexler (1968) and is still a popular tool. FP6 used VAD with a single PPI, while FP2 combined the radial velocity measurements from five PPIs of different elevations before performing the VAD technique on each height bin. This was done to increase vertical resolution and decrease the minimum observation altitude while still resolving the entire depth of the boundary layer. The FP2 winds used in this study are extremely similar to those provided by Carroll and Delgado (2019).

Winds from each instrument were subjected to quality control appropriate for the scan type and retrieval method. The VAD retrieval at FP6 was performed with all lidar measurements, no signal-to-noise ratio (SNR) filtering. The root-mean-square (RMS) difference between the VAD fit and lidar measurements was used to screen the VAD retrievals, omitting any values with $\text{RMS} > 2.0$ m/s. The VAD winds and RMS values are given in Hanesiak and Turner (2016b). The FP2 lidar line-of-sight wind data (Delgado et al., 2016) were initially filtered to omit points below -28.5 -dB SNR, then performing VAD retrieval if at least 30 points remained in the given altitude bin. Then R^2 and RMS of the VAD fit were used for additional quality control, removing points in the wind retrieval that had both an $R^2 < 0.85$ and $\text{RMS} > 2$ m/s for high wind speed (> 10 m/s) or $\text{RMS} > 4$ m/s for low wind speeds (< 10 m/s). The variable RMS threshold accounts for the higher RMS in weak-wind, high-turbulence environments as may be found in the daytime convective boundary layer; the turbulence can result in high RMS despite confidence in accurate retrieval of low horizontal wind speeds. The WINDCUBE[®]70 at FP3 reported winds calculated by proprietary Leosphere software, with a user-determined SNR threshold that varied from -31 to -32 dB depending on the amount of aerosol scatterers present. These wind values are reported as-is from Hanesiak and Turner (2016a). For all sites, periods when rain interfered with wind profiling were removed from the analysis by visual inspection.

Table 1
Doppler Lidar Instrument and Wind Retrieval Parameters for the Three Sites

-	FP2	FP3	FP6
Lidar	Leosphere WINDCUBE® 200S	Leosphere WINDCUBE® 70	Leosphere WINDCUBE® 200S
Owned/operated by	University of Maryland, Baltimore County (Delgado et al., 2016)	University of Manitoba (Hanesiak & Turner, 2016a)	University of Manitoba (Hanesiak & Turner, 2016b)
Scan type	Multiple PPIs	DBS	Single PPI
Scan elevation (°)	5, 7.5, 10, 20, 45	75	60
Profile periodicity ^a	19 or 24 min ^b	15 s	2 min
Minimum altitude (m)	15	100	87
Vertical resolution (m)	15	50	43
Footprint at 500 m AGL	2.7 km (20° scan)	270 m	580 m
Start date	3 June	30 May	8 June
End date	14 July	15 July	15 July

^aFor this research, FP3 and FP6 wind profiles were downsampled by averaging, to match FP2 temporal resolution. ^bVariable during PECAN based on vertical stare duration.

The FP2 Doppler lidar was also used for retrieval of the MLH via the algorithm presented in Bonin et al. (2018). The algorithm uses fuzzy logic to combine several independent retrievals of the MLH utilizing every scan in the lidar's cycle, incorporating both mixing (via turbulent kinetic energy proxy measurements) and tracers for mixing (inferring well-mixed aerosol presence from backscatter intensity).

Rawinsondes were launched at the Doppler lidar sites throughout the PECAN period, often with three or more launched at a given site each night. Launch timing was irregular from night to night and among sites, as dictated by nightly mission goals. Most launches were in the 0000 to 0900 UTC time frame, 2 hr before sunset to 2 hr before sunrise. Figure 2 shows comparison of the retrieved wind fields of each lidar with all coincident co-located rawinsonde profiles. Characteristics of the data and linear regressions are listed in Table 2. Rawinsonde measurements were interpolated to lidar heights, as they are much finer resolution than the lidars (~5-m rawinsonde versus 15- to 50-m lidar). Only heights from the surface up to 2 km are considered, matching the domain of interest for this study. For these Doppler lidar wind field retrievals, a significant spatial and temporal footprint is unavoidable, and the wind vector product assumes homogeneity within the sampling footprint. The FP2 lidar spatial footprint radius can be up to a few kilometers at low altitudes (dependent on SNR) and one wind profile is produced from 12 min of observations. The FP3 lidar has the smallest maximum footprint radius of 265 m at 2 km agl, with 15-s temporal integration. In contrast, the rawinsonde measurements are in situ and reported at 1 Hz (2 Hz for FP6), and their location changes as the balloon drifts with the wind. These instrument sampling differences contribute to the discrepancy between the lidar and rawinsonde data. Overall, data from the Doppler lidars at all three locations compared very well to the rawinsonde measurements.

2.2. In Situ Observations

Data from the 5.66-m level of a short tower at FP2 supplements the Doppler lidar in analysis of the LLJ environment. Turbulent flux of sensible heat was calculated from an integrated sonic anemometer and gas analyzer, using the eddy correlation method with nonoverlapping 30-min averaging. The flux sensors were collocated with a probe to measure air temperature. Data were quality-controlled by the operators considering instrument diagnostics and reasonable physical ranges. The tower instrumentation was operated by scientists from the Naval Postgraduate School, and for this study the data are used as-is from UCAR/National Center for Atmospheric Research (2016).

2.3. Jet Categorization

Classifying LLJs (or NJs) is typically done with criteria similar to that introduced by Bonner (1968). These methods rely on the lower tropospheric wind speed maximum, referred to as the nose or core of the jet, and the shear above, thus detecting the “nose-shaped” profile characteristic of the jet. For this study we take the height of the maximum wind speed below 1.25 km in a given lidar profile. The shear is then calculated as

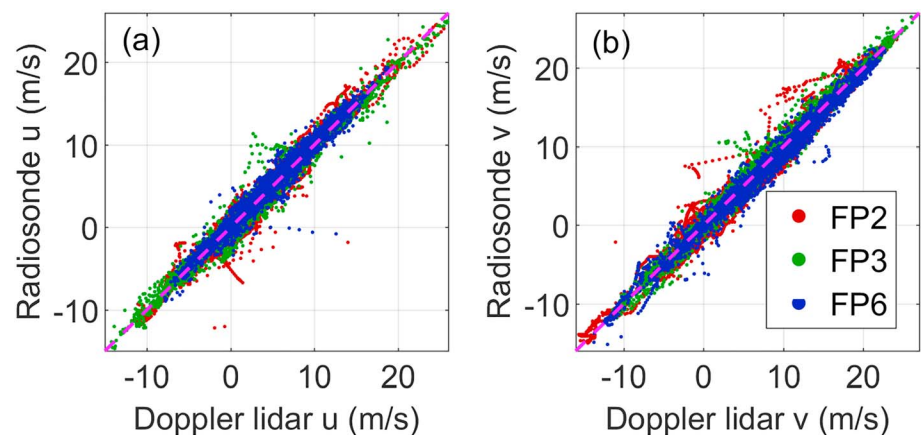


Figure 2. Doppler lidar versus rawinsonde wind components (a) u (westerly) and (b) v (southerly) for all sites. The dashed magenta line is a 1:1 line for reference. Counts and best fit line statistics are in Table 2.

the difference of the nose speed and the minimum speed in the layer above the nose but below 3 km. When a jet is detected, it is sorted into a category denoting the strength of those two criteria, ranging from the weakest, jet-0, up to the strongest, jet-3. Values of the speed maxima (V_{\max}) and upper shear (ΔV) criteria are listed in Table 3. We employ two modifications beyond the Bonner (1968) criteria. One is the addition of a jet-0 category identical to that introduced by Whiteman et al. (1997). Second is a small relaxation of the upper level shear requirement for jet-2 and jet-3. This is necessary because of the limited altitude range of the Doppler lidar data compared to the rawinsonde observations for which these criteria were originally introduced; the lidars were sometimes unable to capture the full shear requirement before losing signal and hence would falsely categorize many strong jets into weaker categories. Visual inspection and rawinsonde comparisons were used to verify the validity of the categorization criteria used here.

Jets defined by these criteria can be further separated by wind direction. We confine the LLJs to having core wind direction between 135° and 315° (i.e., grouping winds that are southerly or westerly), and NJs likewise between 315° and 135° (i.e., northerly or easterly). This separation is made because of the fundamental differences in wind profile evolution, forcing mechanisms, and impacts. The 180° split delineating LLJs and NJs is not divided by 90° and 270° as might be expected (and was used in earlier studies such as Song et al. (2005) and Whiteman et al. (1997)). This is because of the inertial oscillation and downslope acceleration of LLJs occasionally resulting in LLJs with directions reaching 270° late in their life cycle, after veering for several hours. Likewise, NJs were observed veering beyond 90° . The 135° to 315° division makes borderline cases much rarer. Recent publications such as Doubler et al. (2015) and Walters et al. (2014) use a similar division. Nights without jets were divided into the two direction groups by visual inspection, considering dominant wind speed within the lowest 500 m.

Table 2
Statistics of the Data and Linear Regressions for the Doppler Lidar Comparisons to Rawinsondes Shown in Figure 2

	Number of soundings	Number of data points	Line slope	Line y intercept	R^2	RMSE
FP2 u	82	8412	0.995	-0.138 m/s	0.970	0.975 m/s
FP2 v			0.998	0.0571 m/s	0.978	1.10 m/s
FP3 u	130	3883	0.979	0.0078 m/s	0.974	1.01 m/s
FP3 v			1.01	0.0848 m/s	0.985	0.957 m/s
FP6 u	91	3876	0.996	0.307 m/s	0.966	0.906 m/s
FP6 v			0.973	-0.180 m/s	0.980	0.936 m/s

3. Characteristics of Observed Jets

3.1. Time Series of PECAN Winds

Figures 3 and 4 show Doppler lidar wind speed and direction profiles from 20 days at FP2, FP3, and FP6 (the full PECAN time span is in Supporting Information). The diurnal cycle of jets is apparent, as is the veering of nightly LLJ winds expected from IO theory. This is especially clear during the span of 20–25 June with the alternating stronger (nighttime) and weaker (daytime) wind speeds accompanied by nocturnal southerly to westerly veering.

These figures also show the influence of synoptic forcing with multiday periods of strong LLJs (e.g., 20–25 June) or weak winds (e.g., 26–30 June), and similar behavior at all three sites as events often span the

Table 3

Jet Strength Category 0 Through 3 Definitions, and the Number of each that was Observed During PECAN at each FP in this Study. In Parentheses are the Percentages of Occurrence of each Jet Type Out of the Total Observation Nights at the Given Site. The Rows Denoted as FP2, FP3, and FP6 Include LLJ and NJs. The Rows with “SW” Only Count the Subset of each Category that had Southerly or Westerly Winds (i.e. only LLJs and Non-Jet Nights with Southerly or Westerly Winds).

Category	No jet	Jet-0	Jet-1	Jet-2	Jet-3	Total
V_{\max} (m/s)	-	≥ 10	≥ 12	≥ 16	≥ 20	-
ΔV (m/s)	-	≥ 5	≥ 6	≥ 7	≥ 8	-
FP2	7 (17)	10 (24)	3 ^a (7)	5 (12)	16 (39)	41 (100)
FP3	11 (23)	5 (11)	12 (26)	9 (19)	10 (21)	47 (100)
FP6	9 (25)	3 (8)	6 (17)	7 (19)	11 (31)	36 (100)
FP2 SW	2 (5)	5 (12)	2 (5)	4 (10)	16 (39)	29 (71)
FP3 SW	5 (11)	2 (4)	6 (13)	7 (15)	10 (21)	30 (64)
FP6 SW	3 (8)	1 (3)	3 (8)	6 (17)	10 (28)	23 (64)

^aFP2 had three nights that were detected as jet-1, but two of those nights had very poor Doppler lidar data coverage, and hence, FP2 jet-1 nightly statistics are omitted from the rest of this study.

observation domain. Nights with strong LLJs generally correspond to an east-to-west pressure gradient within the boundary layer, as confirmed by surface analysis maps. This east-to-west pressure gradient, with no fronts in the domain, was the most common synoptic setup during the observation period.

Nights of weaker winds are usually caused by cold fronts or stationary fronts blocking the otherwise southerly flow. Fronts heavily influenced the nocturnal flow in at least part of the PECAN domain on 30–31 May; 8, 12–13, 16, 19, 23, and 26–30 June; and 2–3 and 7–10 July. These fronts are responsible for every NJ observed at FP2 and FP6; winds at FP3 tend toward easterly or westerly directions at these times. The exclusive appearance of NJs behind cold fronts during PECAN differs significantly from the findings of Whiteman et al. (1997), who reported only 68% of NJs following cold fronts over a two-year rawinsonde study in north-central Oklahoma. This discrepancy is likely due to the warm-season time span of PECAN versus the all-season inclusion of Whiteman et al. (1997), as the warm season is known to have the strongest and most consistent synoptic setup for generating southerly LLJs.

Outflow from MCSs or smaller precipitation cells rarely interrupted developed LLJs, as indicated by a sudden shift in wind direction and reduction

in wind speed. The only two events that met NJ criteria unrelated to surface fronts were generated by MCS outflow (15 June and 14 July), where cells were present over the FPs at sunset and persisted within the domain through sunrise. Jet features for these two events are less consistent throughout the night than NJs or LLJs driven by synoptic setups. A focused study of all PECAN MCSs is presented in Hitchcock et al. (2019).

3.2. Analysis of Daily Wind Profiles

Table 3 summarizes LLJ and NJ nightly jet classification into one of the four strength categories, with those not meeting the minimum classification criteria grouped together as nonjet nights. For the purpose of this study categories are exclusive, with only the strongest detected category being assigned to a given site on a given night. Two consecutive wind profiles with equal category were required for assignment; this was done to exclude irrelevant transient features. Note that the total number of nights for each site differs due to data availability. Sites were evaluated independently for Table 3, so heterogeneity of a single night or jet event may result in different classifications at different sites.

LLJ-3s were the most common jet type. Almost half of the observation nights at FP2 and FP6 were LLJ-2s or LLJ-3s (49% and 45%, respectively); this number is diminished for the northernmost site FP3 (36%). The only NJ-3 was caused by a cold front just south of FP6 on 7 July; this same event was a weaker NJ-2 at FP2 and FP3, the sites located farther behind the front. Another NJ-2 was only detected at FP3 (23 June), associated with cold front that passed through an hour before sunset. This front reached the other FPs while a southerly LLJ was ramping up and the front interrupted the LLJ but did not form as strong or deep of a NJ profile at these sites. The only other event identified as a NJ-2 was associated with a mesoscale convective system that passed over FP6 on 14 July.

The preferred southerly direction of strong jets disappears with decreasing jet strength category. No clear preference for northerly or southerly alignment is seen for jet-0 or jet-1. Further, most nights without jets have northerly winds, reflecting inhibition of the standard LLJ driving mechanisms. These tendencies could be expected from the well-known aspects of LLJ forcing theories, which rely on the common east-to-west pressure gradient and southerly geostrophic wind to produce the characteristic large IO, along with the diurnal heating and cooling of the sloped Great Plains which necessarily generates southerly nocturnal jet structures.

To further address geographic trends with the percentages in Table 3, we see LLJ-3s most frequently at the southwestern site FP2 and least frequently at the northern site FP3. FP2 also has the highest frequency of southerly winds overall. This pattern agrees with the NARR-derived climatology by Doubler et al. (2015) and the rawinsonde climatology by Bonner (1968), which show FP2 to be closest to the region of maximum southerly LLJ frequency. FP3 and FP6 are north and east of the climatological maximum, respectively.

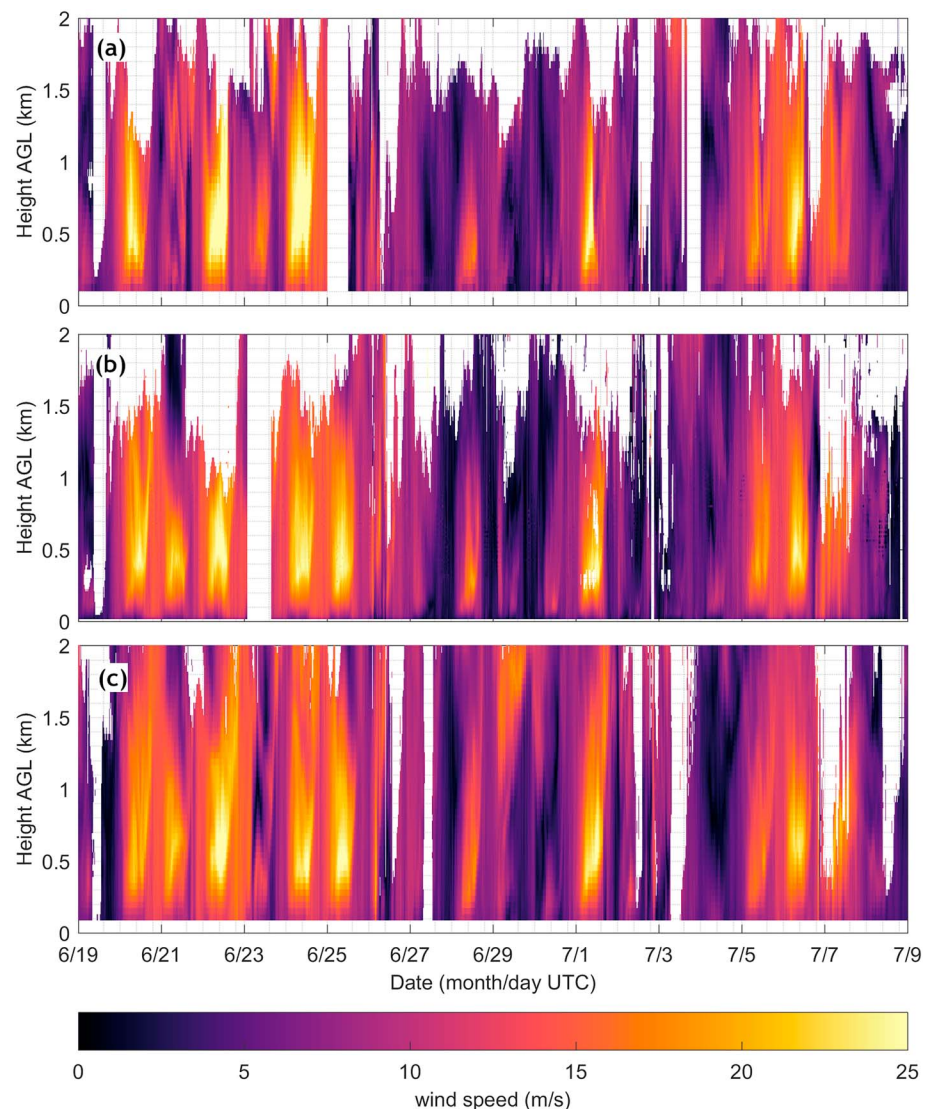


Figure 3. Time series of wind speed profiles from Doppler lidars at (a) FP3, (b) FP2, and (c) FP6 for 19 June through 8 July. White areas indicate data missing or removed by quality control.

Figure 5 reveals the synoptic patterns that were evident in Figures 3 and 4 and highlights important jet characteristics with hourly reports of strength category, wind direction, and nose height for all of PECAN. Most jets live for several hours, ramping up at sunset (~0200 UTC) and dying out 1–5 hr after sunrise (~1120 UTC). The rising CBL in the morning plays an important role in observed LLJ ramp-down. The increased turbulent mixing in this layer erodes the strong LLJ wind speeds, starting near the surface and expanding upward. This interaction could result in substantial downward mixing of atmospheric constituents transported by the LLJ, and thus have important implications for air quality (Robert M. Banta et al., 1998; Delgado et al., 2015; P. M. Klein et al., 2014; Mao & Talbot, 2004). Concerning dynamics, the morning CBL is thus responsible for some of the weakening of LLJ wind speeds and an apparent rising of the LLJ nose as the faster wind speeds remain above the growing CBL. An example of this is shown in Figure 6. This morning rising is most pronounced at FP6 because of the FP6 lidar's relatively large vertical range, resolving the rising jet profile shape beyond what the lower-powered FP3 lidar or shallower-pointing FP2 lidar could observe.

Several of the higher jet noses in the late afternoon are shallow peaks in the wind speed profile that descend at sunset and develop into more prominent LLJs. These satisfy the jet detection criteria because of very low wind speeds above the boundary layer satisfying the shear requirement, and hence, the longer

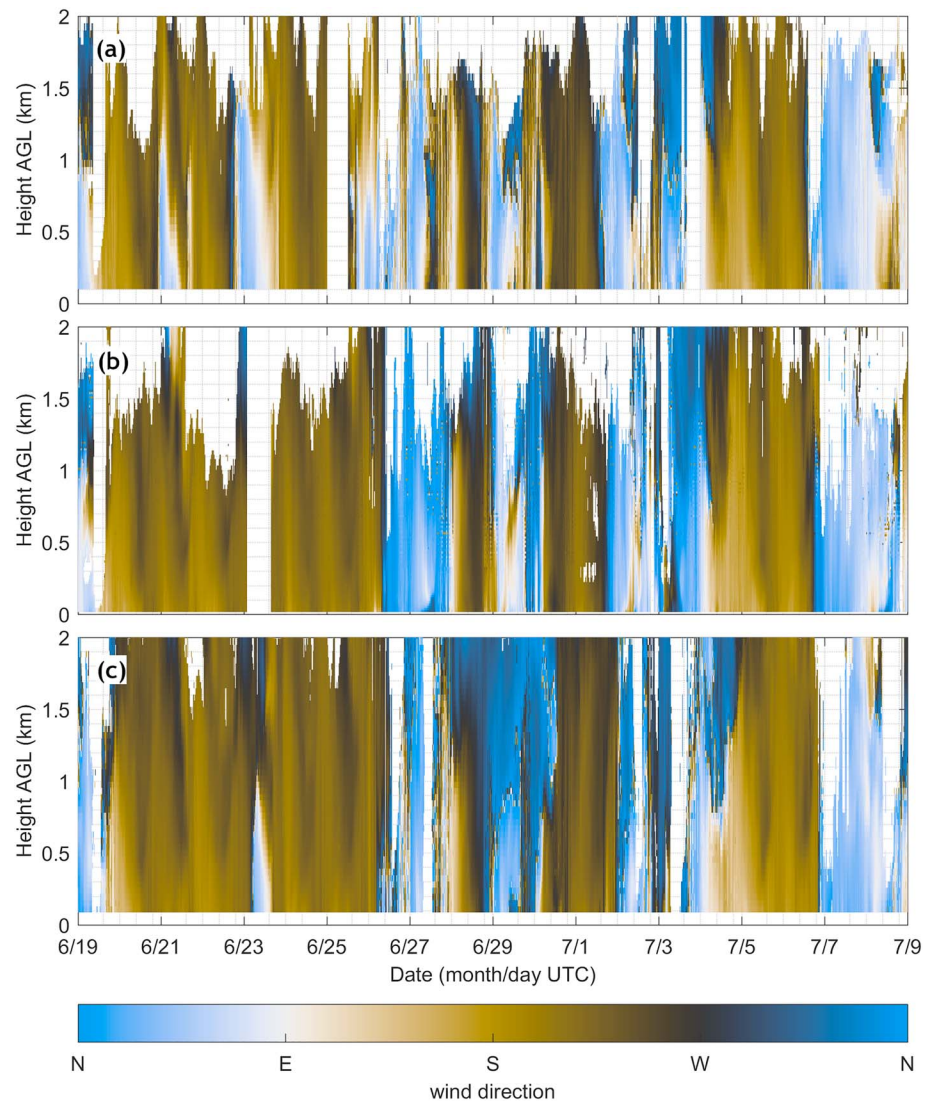


Figure 4. Same as Figure 3 but for wind direction instead of wind speed.

range of the FP6 lidar results in more of these found at FP6 than the other sites. While jet criteria have been observed in the daytime in the literature (e.g., Vanderwende et al., 2015), a common dynamic cause is unknown.

Overall, this hourly analysis perspective shows that wind profiles at FP2 and FP6 were the most similar throughout the campaign. The northernmost site FP3 frequently had significant differences in its wind profile due to interfering fronts, pressure centers, and convective systems that did not simultaneously affect the other sites.

Average LLJ-3 nose heights at each site are presented in Figure 7. FP2 and FP3 had extremely similar mean LLJ-3 nose heights during PECAN despite being separated by 150 km. FP6, located farthest east and at a lower elevation, had a significantly lower average nose height MSL but higher AGL than the other sites. Smith et al. (2019) also reported heterogeneity in LLJ-3 nose height among PECAN FPs, focusing on individual events rather than an average over the PECAN time span. Some past studies with different observation sites have found the nose height of strong LLJs to remain fairly constant with respect to MSL despite changes in terrain height, although the sites in these studies were located closer together than the PECAN FPs (Banta et al., 2002; Song et al., 2005). Weaker LLJs and NJs had much greater nose height variability than LLJ-3s during PECAN. It should also be noted that while the range limitations of FP3 and FP6 lidars limit the

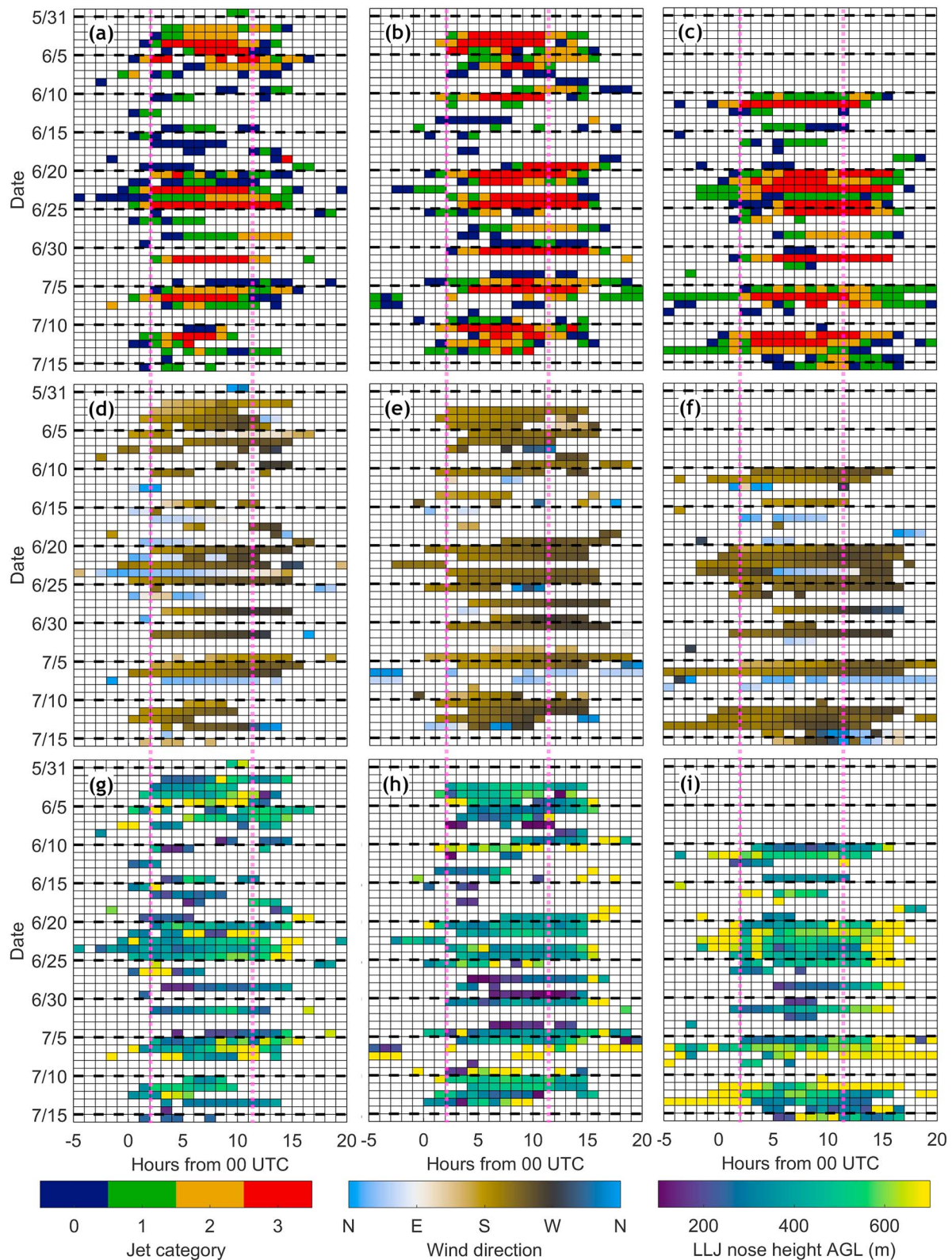


Figure 5. Jet properties over the entirety of PECAN at (a, d, and g) FP3, (b, e, and h) FP2, and (c, f, and i) FP6. Properties displayed are jet category (a–c), wind direction (d–f), and jet nose height (g–i). Color bars are at the bottom of the figure and white spaces are times when no LLJ was observed. In each subfigure, each row shows 24 hr in 1-hr increments. When more than one wind profile was available in an hour, median values from that set are reported. Dashed magenta lines indicate the approximate times of sunset and sunrise.

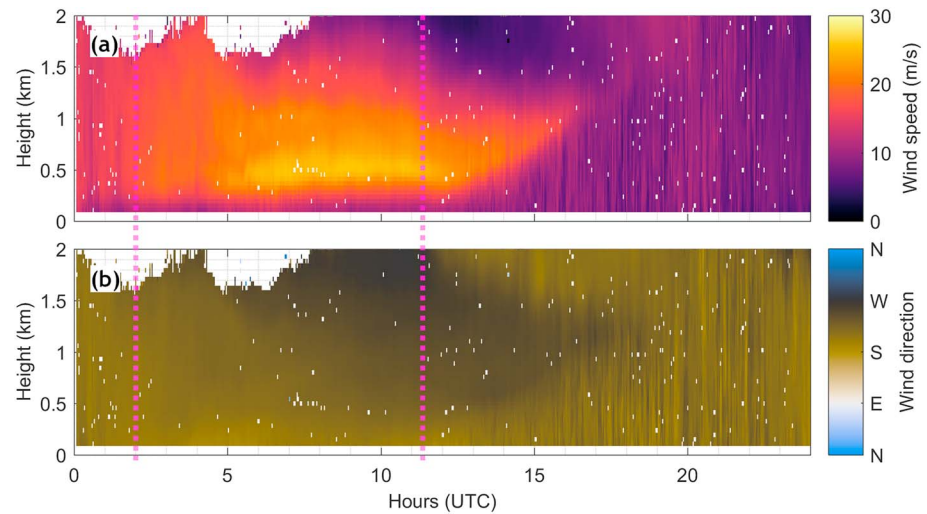


Figure 6. FP6 Doppler lidar (a) wind speed and (b) direction for the 25 June LLJ-3. Magenta lines mark sunset and sunrise. White spots indicate data removed by quality control routines.

lowest observed jet peak to 150 and 130 m, respectively, jet-0 and jet-1 noses at FP2 are occasionally seen below 100 m AGL.

Figures 8 and 9 plot the mean horizontal winds as a function of height and time across all LLJs at FP2, separated by category (excluding LLJ-1 due to insufficient data availability). All directions were included in the nonjet category. The standard deviation of the mean winds is also plotted to explore variability among cases. This combined display of all nights draws out average behavior of each category as well as similarities and differences among the LLJs. Two dates were omitted from these statistics as outliers: 5 June (MCS outflow truncated a developed LLJ-3) and 11 June (exceptionally strong and deep MCS inflow). Corresponding mean MLHs (discussed further in section 3.3) are also plotted and serve as a reference for the LLJ lifetime within the diurnal framework, as the MLH falls and rises around sunset and sunrise, respectively.

The mean LLJ features occupy the nocturnal boundary layer and impinge on the evening and morning convective boundary layers. LLJ-3s tend to be strongly synoptically driven and thus last from early evening to midmorning, reaching peak wind speed shortly after midnight (5 UTC). LLJ-2s can be similarly long-lived but were often observed with slower or later ramp-up during PECAN, contributing to the relatively late peak of Figure 8e. Three of the four LLJ-2s (6, 10, and 28 June) reached maximum speed at FP2 after sunrise. LLJ-0s were on average the shortest-lived category, and showed no clear preference for timing early or late in the night (NJ-0s were similar in this regard). This variable timing is responsible for the LLJ-0 mean profiles of Figure 8c not exceeding 10 m/s. For each LLJ category the mean wind direction veers with time, in accordance with IO theory.

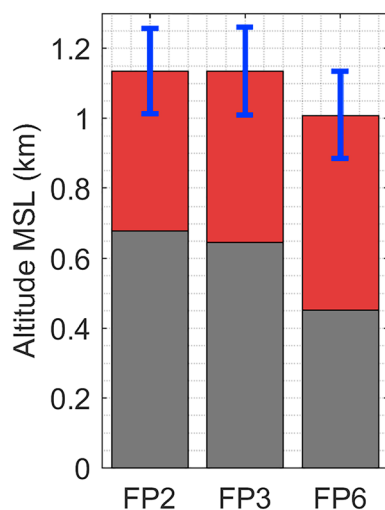


Figure 7. Mean LLJ-3 nose heights in MSL at each site over the entire PECAN time span, with standard deviation bars. Terrain height at each site is in gray.

The standard deviation plots are a powerful tool for drawing out similarities and differences among the nights. Low standard deviation values in Figure 9h indicate that LLJ-3 wind direction among events is almost invariant in the evening boundary layer and throughout the night, until after sunrise. LLJ-3 wind speed variability in Figure 8h is lowest in the evening and onward until midnight, indicating the common characteristic nature of the synoptic setup forcing these jets. The LLJ-3 wind speed variability also shows a minimum region close to the surface between sunset and sunrise, indicating very similar profiles in the high-shear region near the surface, where surface friction is a limiting factor. This minimum region is also present for weaker LLJ categories, although it is less

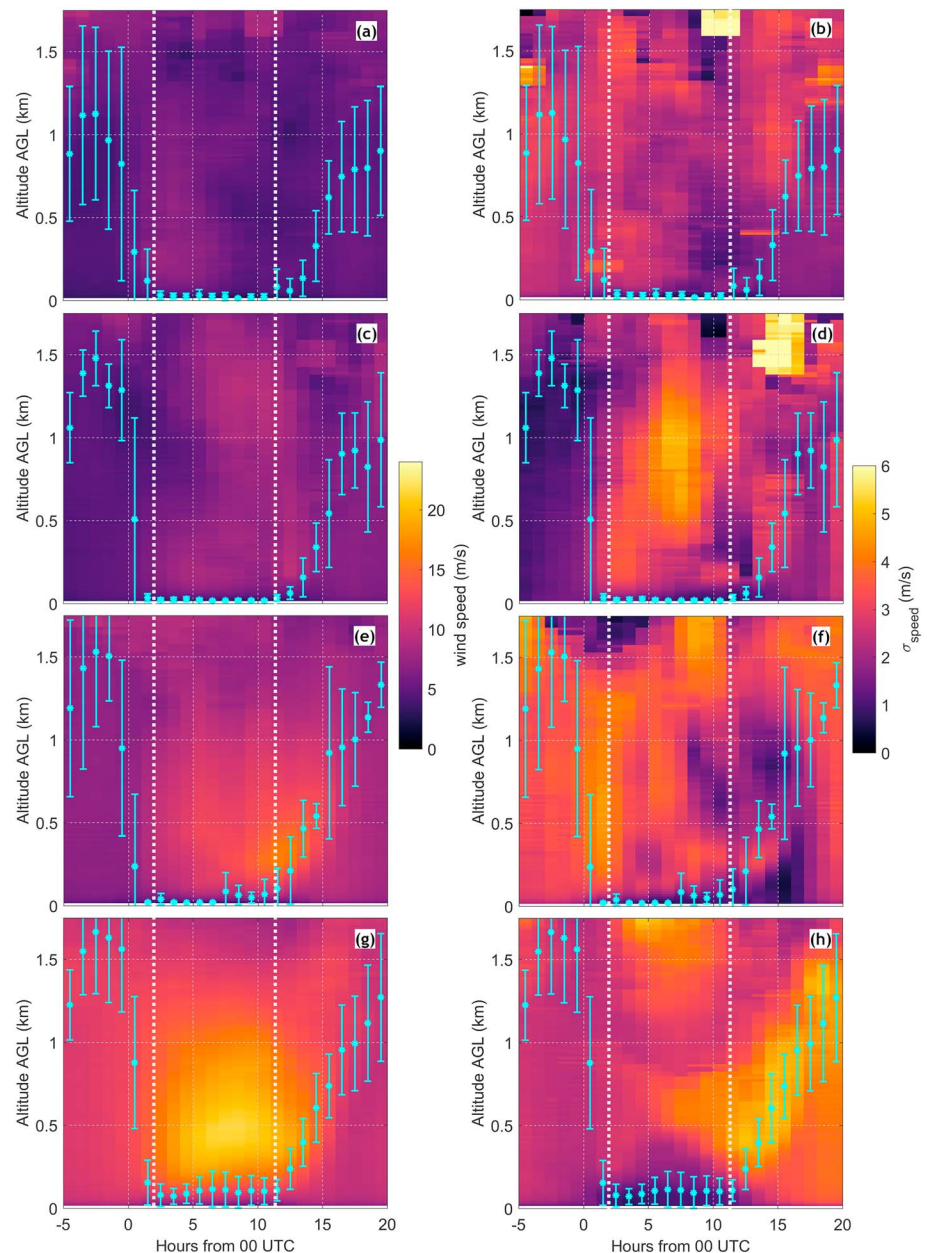


Figure 8. Mean LLJ wind profiles by hour UTC for PECAN FP2, separated by LLJ category: (a and b) nonjet nights, (c and d) LLJ-0, (e and f) LLJ-2, and (g and h) LLJ-3. Only southerly LLJs are included here, except nonjet plots that include all directions. (a), (c), (e), and (g) are the mean wind speed and (b), (d), (f), and (h) are the standard deviations of the values that contributed to each mean speed. A rolling time average is used, reporting profiles averaged over 3 hr with 1-hr resolution. Cyan points are mean MLHs from Doppler lidar, with standard deviation bars, calculated with the same averaging method as winds except just 1-hr windows instead of 3-hr to avoid smoothing the sharp gradients present at transition periods. White dashed lines mark sunset and sunrise.

pronounced. Greater wind speed variability for LLJ-3 begins at midnight just above the mean nose height. This localized variability in the profile then broadens to lower and higher altitudes, eventually showing no strong similarity in the entire late morning boundary layer. Thus, overall, LLJ-3s develop under extremely similar conditions, but after reaching their peak speed around 5–7 UTC the wind speed profile evolutions can differ, either experiencing substantial ramp-down before sunrise or persisting with strong winds beyond sunrise. The farthest outliers in this sense were two LLJ-3s (20 June and 1 July) that did not reach their high maximum speeds (>25 m/s) until 10 UTC, hours later than most other LLJ-3s. We

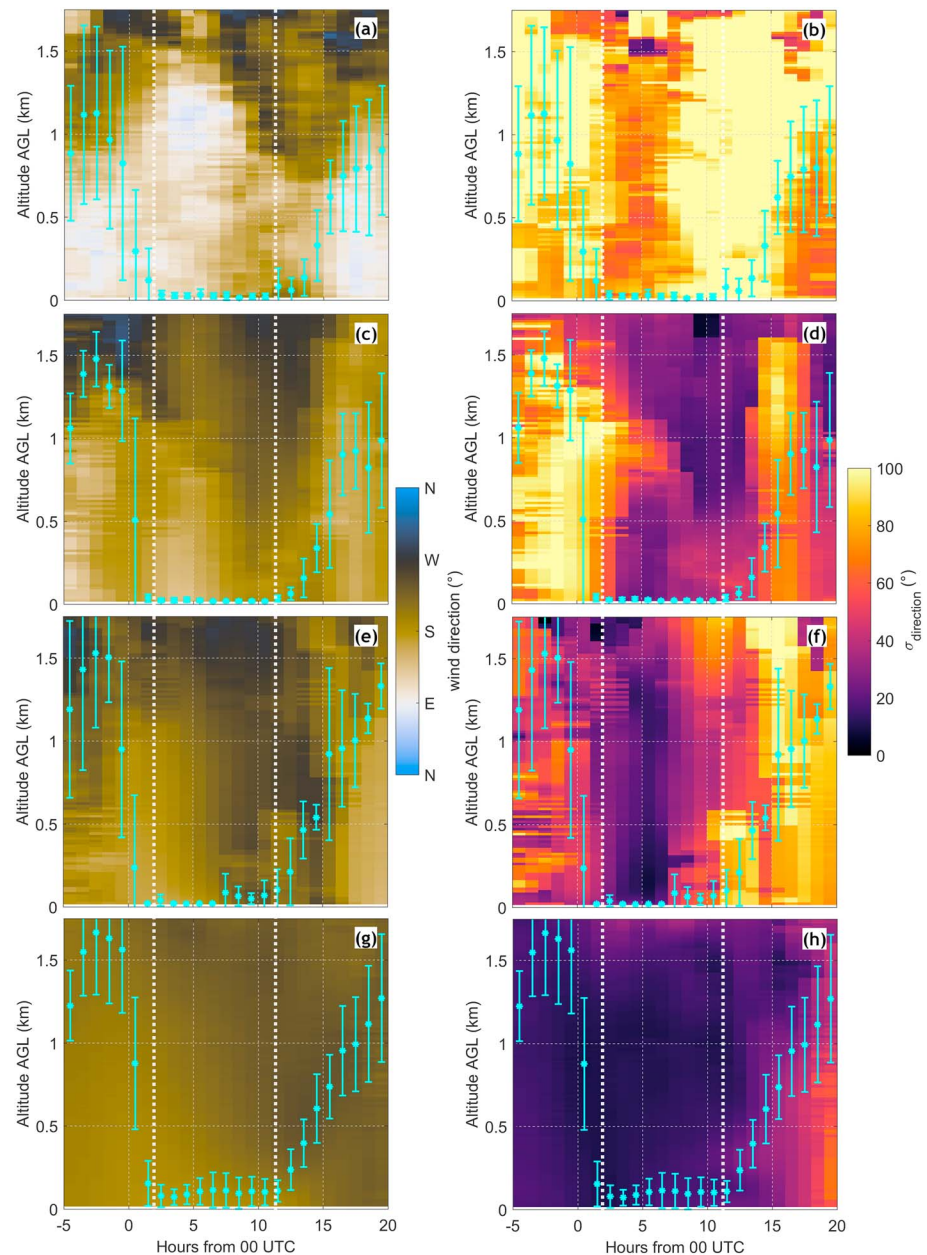


Figure 9. Same as in Figure 8 but wind direction instead of wind speed.

also note that there is high variability in LLJ-3 wind speed above 1.2 km during the night, which indicates spread among the above-nose shear profiles. The other categories of LLJ suffer from relatively limited sampling at FP2 and we are unable to make further clear interpretations.

Although Figures 8 and 9 only examine southerly LLJs at FP2, the same plots were made for FP3 and FP6 LLJs as well as NJs at the three sites (not shown here due to space limitations). Given the time span of PECAN, this approach of dividing into 10 different types suffers from poor sampling of some types, but some conclusions can still be drawn:

FP2 and FP6 show very similar characteristics in the structure and evolution of their LLJ plots. Minor differences are present for LLJ-3s, with FP6 profiles slightly deeper. FP6 LLJ-3s have a similar wind speed standard deviation pattern to FP2 except the high variability at nose height begins later, at 9 UTC. The only major difference in wind speed across all categories is for LLJ-2. For this category, the wind speed peaks

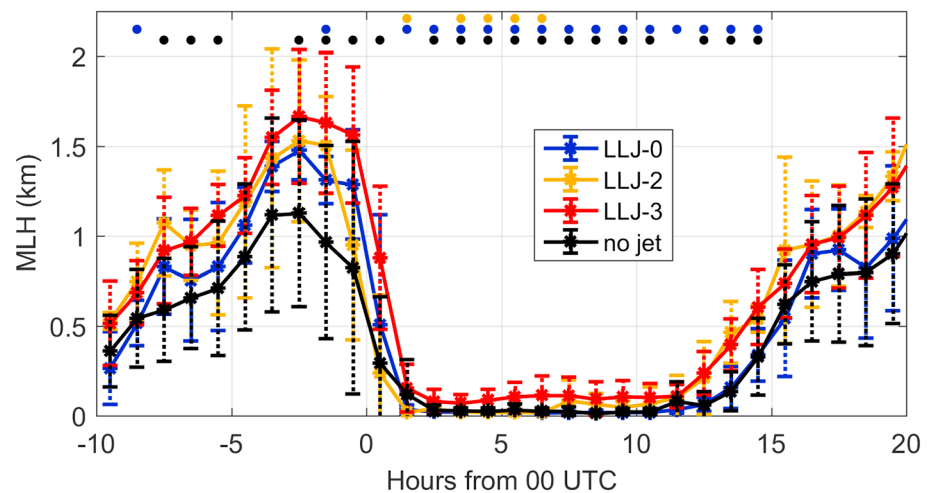


Figure 10. Hourly means and standard deviations of MLHs separated by LLJ category, as shown in Figures 8 and 9.

at FP6 between 06 and 13 UTC, while at FP2 the wind speed maxima are observed later (9–13 UTC). A longer period of study or detailed examination of the driving mechanisms of each LLJ would be needed to determine if this is typical or can be attributed to sparse sampling of LLJ-2s during PECAN. In the standard deviation of wind speeds for LLJ-2 cases both sites have high variability before 5 UTC, but FP6 has an additional peak later on (between 12 and 15 UTC and from 450 to 950 m AGL) because some jets experienced earlier ramp-down.

FP3 exhibited much more variability in LLJ-2 and LLJ-3 wind speed and direction than FP2 or FP6 due to its location farther north. Many LLJ-2s and LLJ-3s that would be long-lived were interrupted by fronts or precipitation and outflow. For NJs, no organized patterns emerged between sites or categories.

FP2 and FP6 can be used to address along-slope LLJ heterogeneity. As listed in Table 3, a greater percentage of nights at FP2 had LLJ-3s, agreeing with the findings of stronger LLJs at western sites by Smith et al. (2019). The diagonal striations presented in Gebauer et al. (2018) and Smith et al. (2019) are not apparent in the mean LLJ wind profiles at any site because these striations are not found in all LLJs and they are weak features with variable timing. Visual inspection of the winds from each night revealed diagonal striations to be most common at FP6, present there in half of the LLJ-3s.

3.3. Evolution of Mixed Layer Depth Associated With LLJs

The MLHs plotted in Figures 8 and 9 are plotted on a single set of axes in Figure 10. Figure 11 shows the individual daily MLHs that contributed to the means and standard deviations. An unequal variance *t* test with a $p < 0.05$ threshold was applied to the hourly MLHs to assess the statistical significance of the apparently different mean values for each jet category. The markers at the top of Figure 10 show *t* test results of LLJ-3 MLHs against each other category. The MLHs are different between LLJ-3 and nonjets in a statistically significant way for most hours. Conversely, LLJ-3 MLHs versus LLJ-0 or LLJ-2 have few instances of statistical significance, especially during the daytime. However, daytime *p* values of LLJ-3 versus LLJ-0 MLHs were fairly low (<0.175), suggesting that this might resolve as a statistically significant difference if more data were available. Mean MLHs for other category combinations (e.g., LLJ-2 versus nonjets) were not significantly different.

Examining the MLHs in Figures 8–11 reveals three clear patterns: (1) higher category LLJs are preceded by stronger wind speeds in the CBL, (2) higher category LLJs follow deeper MLHs, and (3) MLH begins falling from a rising or steady CBL height toward nocturnal heights at a later time for LLJ-3s.

The strong CBL winds of point (1) imply greater geostrophic forcing for stronger LLJs. Klein et al. (2016) used the afternoon CBL wind speed as a scaling factor that correlates with the geostrophic wind speed, particularly in the context of LLJs and the ageostrophic afternoon flow that precedes inertial oscillation.

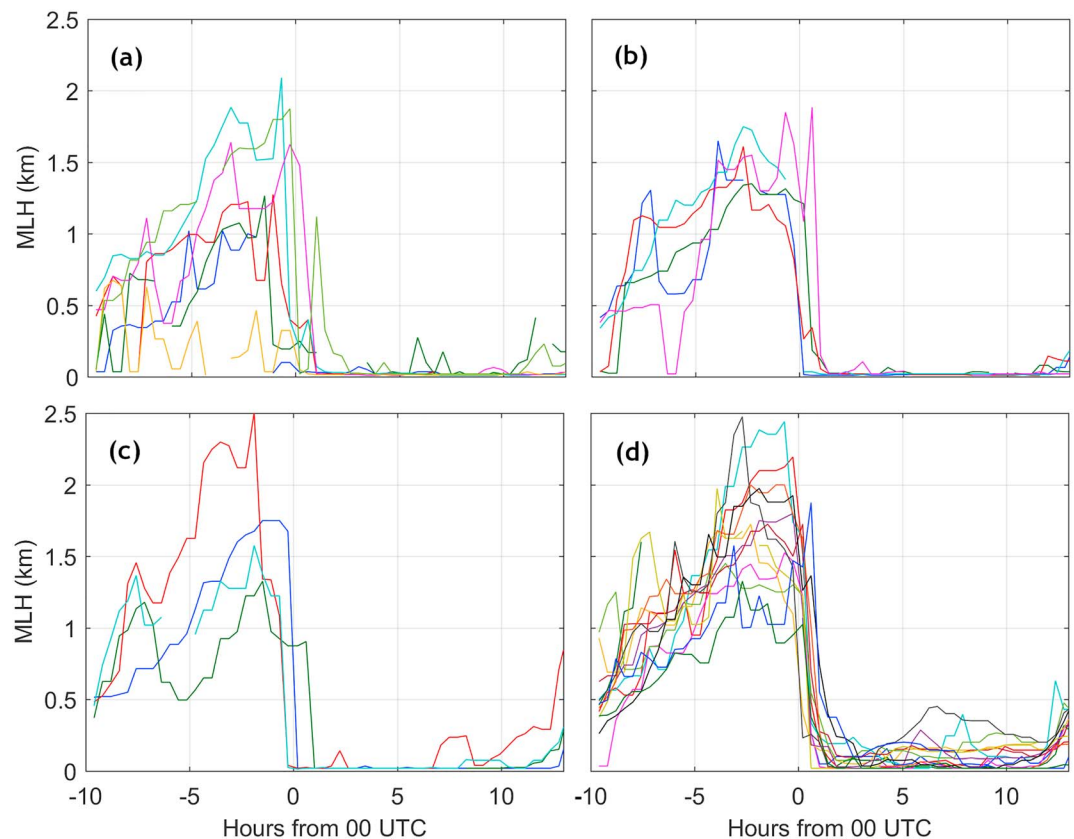


Figure 11. Plots of the individual MLHs contributing to Figure 10, with time axis range focusing on the nocturnal period and the preceding CBL. Nonjet, LLJ-0, LLJ-2, and LLJ-3 events are shown, respectively, in (a)–(d). Line color is arbitrarily different for each event.

The height differences of point (2) can be generated from a variety of factors and are most likely driven by a combination of influences. Most explicit is the sensible heat flux shown in Figure 12a; LLJ-3s have statistically significant higher sensible heat flux than nonjets and LLJ-0s for most hours of the preceding day. In short, days preceding stronger LLJs have greater sensible heat flux, and thus more heating and buoyant lifting from the surface leading to a deeper MLH. This heating is apparent in the temperature time series (Figure 12b), although temperature versus LLJ category may also be influenced by temperature advection as the persistent southerly winds during periods of consecutive strong LLJs warm the Great Plains region. In contrast, weak or nonjet nights primarily occur following a cold front or when a stationary front in the southern Great Plains is blocking southerly flow. Warmer BL air typically creates deeper MLHs, so temperature advection can contribute to point (2). It may also be possible that kinetic energy of the stronger afternoon winds (i.e., from point (1)) gets transferred into the CBL's turbulent eddies. This increased turbulent kinetic energy (TKE) could expand the ML, but we expect that this contribution would be minor compared to the buoyancy-driven component.

Point (3) could have important implications for IO theory and LLJ development, but more details are needed addressing the cause of the observed pattern and the decay of TKE as a function of time and height. IO is usually theoretically treated as coming from an immediate removal of daytime BL friction (e.g., Du & Rotunno, 2014; Shapiro et al., 2016), which results in acceleration of the ageostrophic wind vector. If this friction is instead gradually reduced, the wind vector can approach geostrophic value before undergoing free IO (effectively a damping mechanism on the IO magnitude). A deep CBL dropping very quickly (as we see for LLJ-3) closely matches the common theoretical assumption and maximizes the IO effect. Further study is needed to test these hypotheses because the MLH algorithm used here identifies the surface-connected mixing layer, and thus a sudden drop in MLH could be due to a local decrease in turbulence near the surface and not throughout the entire boundary layer. Exploring the decay of turbulence versus height would require an

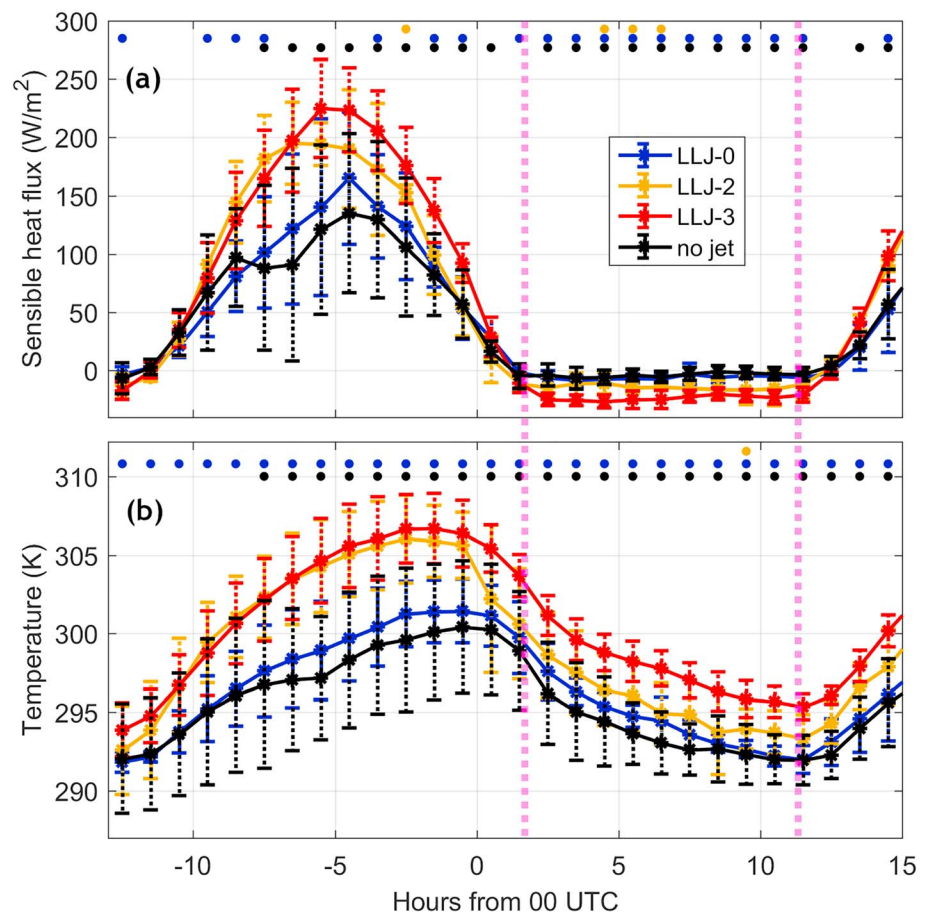


Figure 12. Mean and standard deviation of hourly (a) sensible heat flux and (b) temperature from the 5.66-m tower at FP2, separated by LLJ category. Time span includes the LLJ night, preceding CBL, and following morning transition.

in-depth evening transition study and is beyond the scope of this paper, and may be beyond the capability of the FP2 Doppler lidar because its 50-m range gate size cannot resolve smaller turbulent eddies.

LLJs are known to generate mixing near the surface due to wind shear (Bonin et al., 2015; Sun et al., 2012; Van de Wiel et al., 2012). MLHs only appear marginally higher at night for LLJ-3s, and stay extremely near-surface for the other categories in this study, because the MLH algorithm was parameterized for the relatively strong mixing of the daytime CBL; weaker nocturnal mixing is generally below the detection threshold. Figure 11 shows that some of the LLJ-3s had sustained shallow mixing overnight, whereas others feature sporadic bursts of deeper MLHs. This could be explored beyond the scope of this paper by adjusting the detection threshold of the MLH algorithm and incorporating other data sets.

4. Jet Association With Pristine Nocturnal Convective Initiation

While in-depth case studies of PECAN LLJs influencing CI have been published (Gebauer et al., 2018; Reif & Bluestein, 2017; Shapiro et al., 2018; Trier et al., 2017), we present here jet coincidence with PNCI for the entire PECAN campaign. This is not meant to be an exhaustive study, but rather a brief opportunistic presentation of a known important jet impact, made available by the preceding work of categorizing the jets. The PNCI events used here are a subset (taking only the PECAN time span) of those identified from radar by Stelten and Gallus (2017), and thus, we adopt their definition of PNCI as CI occurring between 0000 and 1200 UTC that is not a direct product of surface features or preexisting convection.

Figure 13 shows all PNCI events during PECAN binned by jet category and direction, and separated into the northern, central, and southern regions of the Plains as defined in Stelten and Gallus (2017, Figure 1). A

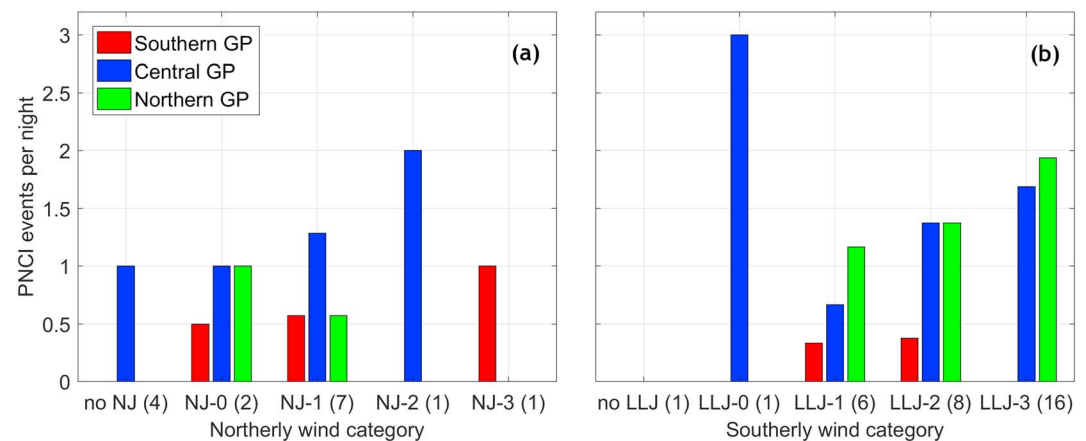


Figure 13. Average number of PNCI events per night separated by regions from Stelten and Gallus (2017), paired with jet category for (a) northerly and (b) southerly winds. Numbers in parentheses on the x axis denote the number of nights of each type of jet.

single jet type is assigned to the whole region on each night. Many nights had the same jet type at all three sites; on nights where this was not the case, the type was assigned as the highest observed category among the three FPs. By this criterion, sampling of LLJ-0s, NJ-2s, NJ-3s, and nonjet nights was sparse during PECAN and thus could be more representative of cases than general behavior, but patterns emerge when focusing on the better-sampled categories. For LLJs, as category increases there is an increase in the number of PNCI events per night and these events shift northward. This unique analysis complements the conclusions of the climatology by Reif and Bluestein (2017), who found that CI is more likely to occur north of an LLJ center although they did not pair this location analysis with LLJ category. Similarly the reanalysis climatology by Berg et al. (2015) found maximum precipitation in the north and central Great Plains when there is an LLJ, but again did not separate this by LLJ strength category. For NJs in Figure 13a there are fewer PNCI events per night than for strong LLJs, and only a slight preference for the central Plains is present.

5. Summary and Conclusions

In this study, time series of Doppler lidar wind profiles were used to examine features of the LLJ in detail with considerations of single events up through mesoscale and synoptic-scale characteristics. Data from three sites spread across Kansas during PECAN included 30 LLJ events over 47 days, capturing heterogeneities in the nightly wind field over the domain and revealing similarities and differences among LLJs separated by strength categories. At one of these sites, the interplay of LLJ dynamics with the CBL and ML was investigated using a recently developed Doppler lidar MLH retrieval algorithm and surface measurements.

The prevalence of periods of several consecutive nights with either strong LLJs or weak and nonjet nights reveals the LLJ to be a synoptically forced mesoscale phenomenon. The two southern sites, FP2 and FP6, showed very similar wind profiles throughout PECAN while FP3, located over 100 km north, frequently differed due to the influence of fronts or convective systems that did not reach the southern sites until later, if at all. All NJs observed during PECAN were located north of cold or stationary fronts. LLJ heterogeneities such as in Smith et al. (2019) were less apparent in this analysis, mainly due to inconsistent presence and timing that vanishes in averaged fields.

LLJ-3s formed with very similar wind profiles in the preceding CBL and during ramp-up, only showing greater variability among cases after reaching peak speed around midnight local time. Weaker jets do not show a clear pattern of this nature, suggesting greater flexibility in how weaker jets form and evolve. Weaker jets also tend to be shorter-lived than LLJ-3s. Three LLJ-2s reached maximum speed at FP2 after sunrise; the driving mechanisms of these events warrant further investigation.

Afternoon MLHs were found to correlate with LLJ strength categories, with LLJ-3s having the deepest preceding MLHs on average. The LLJ categories also correlate with greater surface heat fluxes and surface

temperatures, as expected. Wind speed in the preceding afternoon ML increases with increasing LLJ category, implying greater geostrophic forcing which can produce larger LLJ maximum wind speeds. The MLH algorithm also reveals a shallow mixed layer sustained overnight by LLJ-3s, along with a tendency for LLJ-3s to maintain a deep evening MLH until a later time than weaker category jets.

Comparing jet direction and category to location and number of PNCI events suggests that stronger LLJs are linked to more PNCI and that this PNCI occurs farther north.

While the 47 days of PECAN observations included in this study were sufficient to draw many conclusions and provide a detailed picture of LLJ wind evolution, the value of a longer multisite Doppler lidar study is apparent. Some techniques used here suffered from poor sampling of the rarer jet types, namely, NJs and weak LLJs for the PNCI comparison to jet type and for the mean and standard deviation of jet wind fields. Along with a longer period of study and more sites with Doppler lidars, expanding this research would benefit from choosing Doppler lidar scan routines that allow for robust retrievals of MLH or TKE with a high repetition rate. Having multiple sites with continuous MLH observations could reveal any spatial heterogeneity of the MLH, which might influence LLJ heterogeneity. Doppler lidars with shorter range gates may be preferred for their ability to resolve smaller turbulent eddies in the nocturnal boundary layer. A detailed study of the decay of the TKE profile during the evening transition period could provide new insight into LLJ ramp-up related to IO theory.

Acknowledgments

This work was funded by National Science Foundation award (AGS-1503563) to the University of Maryland, Baltimore County and the NASA Minority University Research and Education Project IRO NNX15AQ03A. B. Demoz was also funded through NOAA Cooperative Science Center in Atmospheric Sciences and Meteorology, funded by the Educational Partnership Program at NOAA in collaboration with Howard University. All data used for this research are in the PECAN archive managed by NCAR/EOL under the sponsorship of the National Science Foundation, https://data.eol.ucar.edu/master_list/?project=PECAN. The FP2 Doppler lidar mixed layer product is not archived. We thank all PECAN participants for their efforts and Sean Stelten and William Gallus for providing their logs of convective events. Color-blind-safe wind direction plots were designed by Peter Kovesi, "Good Colour Maps: How to Design Them," arXiv:1509.03700 [cs.GR] 2015.

References

- Anderson, C. J., & Arritt, R. W. (2001). Representation of summertime low-level jets in the Central United States by the NCEP-NCAR reanalysis. *Journal of Climate*, 14(2), 234–247. [https://doi.org/10.1175/1520-0442\(2001\)014<0234:ROSLJ>2.0.CO;2](https://doi.org/10.1175/1520-0442(2001)014<0234:ROSLJ>2.0.CO;2)
- Arritt, R. W., Rink, T. D., Segal, M., Todey, D. P., Clark, C. a., Mitchell, M. J., & Labas, K. M. (1997). The Great Plains low-level jet during the warm season of 1993. *Monthly Weather Review*, 125(9), 2176–2192. [https://doi.org/10.1175/1520-0493\(1997\)125<2176:TGPLLJ>2.0.CO;2](https://doi.org/10.1175/1520-0493(1997)125<2176:TGPLLJ>2.0.CO;2)
- Banta, R. M., Newsom, R. K., Lundquist, J. K., Pichugina, Y. L., Coulter, R. L., & Mahrt, L. (2002). Nocturnal low-level jet characteristics over Kansas during cases-99. *Boundary-Layer Meteorology*, 105(2), 221–252. <https://doi.org/10.1023/A:1019992330866>
- Banta, R. M., Pichugina, Y. L., & Brewer, W. A. (2006). Turbulent velocity-variance profiles in the stable boundary layer generated by a nocturnal low-level jet. *Journal of the Atmospheric Sciences*, 63(11), 2700–2719. <https://doi.org/10.1175/JAS3776.1>
- Banta, R. M., Pichugina, Y. L., & Newsom, R. K. (2003). Relationship between low-level jet properties and turbulence kinetic energy in the nocturnal stable boundary layer. *Journal of the Atmospheric Sciences*, 60(20), 2549–2555. [https://doi.org/10.1175/1520-0469\(2003\)060<2549:RBLJPA>2.0.CO;2](https://doi.org/10.1175/1520-0469(2003)060<2549:RBLJPA>2.0.CO;2)
- Banta, R. M., Senff, C. J., White, A. B., Trainer, M., McNider, R. T., Valente, R. J., et al. (1998). Daytime buildup and nighttime transport of urban ozone in the boundary layer during a stagnation episode. *Journal of Geophysical Research*, 103(D17), 22,519–22,544. <https://doi.org/10.1029/98JD01020>
- Barandiaran, D., Wang, S. Y., & Hilburn, K. (2013). Observed trends in the Great Plains low-level jet and associated precipitation changes in relation to recent droughts. *Geophysical Research Letters*, 40, 6247–6251. <https://doi.org/10.1002/2013GL058296>
- Berg, L. K., Riihimaki, L. D., Qian, Y., Yan, H., & Huang, M. (2015). The low-level jet over the southern great plains determined from observations and reanalyses and its impact on moisture transport. *Journal of Climate*, 28(17), 6682–6706. <https://doi.org/10.1175/JCLI-D-14-00719.1>
- Blackadar, A. K. (1957). Boundary layer wind maxima and their significance for the growth of nocturnal inversions. *Bulletin of the American Meteorological Society*, 38(5), 283–290. <https://doi.org/10.1175/1520-0477-38.5.283>
- Bonin, T. A., Blumberg, W. G., Klein, P. M., & Chilson, P. B. (2015). Thermodynamic and turbulence characteristics of the Southern Great Plains nocturnal boundary layer under differing turbulent regimes. *Boundary-Layer Meteorology*, 157(3), 401–420. <https://doi.org/10.1007/s10546-015-0072-2>
- Bonin, T. A., Carroll, B. J., Hardesty, R. M., Brewer, W. A., Hajny, K., Salmon, O. E., & Shepson, P. B. (2018). Doppler lidar observations of the mixing height in Indianapolis using an automated composite fuzzy logic approach. *Journal of Atmospheric and Oceanic Technology*, 35(3), 473–490. <https://doi.org/10.1175/JTECH-D-17-0159.1>
- Bonner, W. D. (1968). Climatology of the low level jet. *Monthly Weather Review*, 96(12), 833–850. [https://doi.org/10.1175/1520-0493\(1968\)096<0833:COTLLJ>2.0.CO;2](https://doi.org/10.1175/1520-0493(1968)096<0833:COTLLJ>2.0.CO;2)
- Browning, K. A., & Wexler, R. (1968). The determination of kinematic properties of a wind field using Doppler radar. *Journal of Applied Meteorology*, 7(1), 105–113. [https://doi.org/10.1175/1520-0450\(1968\)007<0105:tdokpo>2.0.co;2](https://doi.org/10.1175/1520-0450(1968)007<0105:tdokpo>2.0.co;2)
- Carroll, B., & Delgado, R. (2019). FP2 UMBC Doppler Lidar Horizontal Winds. Version 1.0 [Data set]. UCAR/NCAR - Earth Observing Laboratory. Accessed 24 July 2019. <https://doi.org/10.26023/M2WJ-994Y-9X0N>
- Delgado, R., Carroll, B., & Demoz, B. (2016). FP2 UMBC Doppler Lidar Line of Sight Wind Data. Version 1.1 [Data set]. UCAR/NCAR - Earth Observing Laboratory. Accessed 29 May 2017. <https://doi.org/10.5065/d6q81b4h>
- Delgado, R., Rabenhorst, S. D., Demoz, B. B., & Hoff, R. M. (2015). Elastic lidar measurements of summer nocturnal low level jet events over Baltimore, Maryland. *Journal of Atmospheric Chemistry*, 72(3–4), 311–333. <https://doi.org/10.1007/s10874-013-9277-2>
- Doubler, D. L., Winkler, J. A., Bian, X., Walters, C. K., & Zhong, S. (2015). An NARR-derived climatology of southerly and northerly low-level jets over North America and coastal environs. *Journal of Applied Meteorology and Climatology*, 54(7), 1596–1619. <https://doi.org/10.1175/JAMC-D-14-0311.1>
- Du, Y., & Rotunno, R. (2014). A simple analytical model of the nocturnal low-level jet over the Great Plains of the United States. *Journal of the Atmospheric Sciences*, 71(10), 3674–3683. <https://doi.org/10.1175/JAS-D-14-0060.1>
- Fedorovich, E., Gibbs, J. A., & Shapiro, A. (2017). Numerical study of nocturnal low-level jets over gently sloping terrain. *Journal of the Atmospheric Sciences*, 74(9), 2813–2834. <https://doi.org/10.1175/JAS-D-17-0013.1>

- Gebauer, J. G., Fedorovich, E., & Shapiro, A. (2017). A 1D theoretical analysis of northerly low-level jets over the Great Plains. *Journal of the Atmospheric Sciences*, 74(10), 3419–3431. <https://doi.org/10.1175/jas-d-16-0333.1>
- Gebauer, J. G., Shapiro, A., Fedorovich, E., & Klein, P. (2018). Convection initiation caused by heterogeneous low-level jets over the Great Plains. *Monthly Weather Review*, 146(8), 2615–2637. <https://doi.org/10.1175/mwr-d-18-0002.1>
- Geerts, B., Parsons, D., Ziegler, C. L., Weckwerth, T. M., Biggstaff, M. I., Clark, R. D., et al. (2017). The 2015 plains elevated convection at night field project. *Bulletin of the American Meteorological Society*, 98(4), 767–786. <https://doi.org/10.1175/BAMS-D-15-00257.1>
- Hanesiak, J., & Turner, D. (2016a). FP3 University of Manitoba Doppler Lidar Wind Profile Data. Version 1.0 [Data set]. UCAR/NCAR - Earth Observing Laboratory. Accessed 30 May 2017. <https://doi.org/10.5065/d60863p5>
- Hanesiak, J., & Turner, D. (2016b). FP6 University of Manitoba Doppler Lidar VAD Winds Data. Version 2.0 [Data set]. UCAR/NCAR - Earth Observing Laboratory. Accessed 30 May 2017. <https://doi.org/10.5065/d64f1ntn>
- Helfand, H. M., & Schubert, S. D. (1995). Climatology of the simulated Great Plains low-level jet and its contribution to the continental moisture budget of the United States. *Journal of Climate*, 8(4), 784–806. [https://doi.org/10.1175/1520-0442\(1995\)008<0784:COTSGP>2.0.CO;2](https://doi.org/10.1175/1520-0442(1995)008<0784:COTSGP>2.0.CO;2)
- Higgins, R. W., Yao, Y., Yarosh, E. S., Janowiak, J. E., & Mo, K. C. (1997). Influence of the great plains low-level jet on summertime precipitation and moisture transport over the central United States. *Journal of Climate*, 10(3), 481–507. [https://doi.org/10.1175/1520-0442\(1997\)010<0481:IOTGPL>2.0.CO;2](https://doi.org/10.1175/1520-0442(1997)010<0481:IOTGPL>2.0.CO;2)
- Hitchcock, S. M., Schumacher, R. S., Herman, G. R., Coniglio, M. C., Parker, M. D., & Ziegler, C. L. (2019). Evolution of pre- and post-convective environmental profiles from mesoscale convective systems during PECAN. *Monthly Weather Review*, 147(7), 2329–2354. <https://doi.org/10.1175/mwr-d-18-0231.1>
- Holton, J. R. (1967). The diurnal boundary layer wind oscillation above sloping terrain. *Tellus*, 19(2), 199–205. <https://doi.org/10.1111/j.2153-3490.1967.tb01473.x>
- Houze, R. A. Jr. (2004). Mesoscale convective systems. *Reviews of Geophysics*, 42, RG4042. <https://doi.org/10.1029/2004RG000150>
- Hu, X. M., Klein, P. M., Xue, M., Lundquist, J. K., Zhang, F., & Qi, Y. (2013). Impact of low-level jets on the nocturnal urban heat island intensity in Oklahoma City. *Journal of Applied Meteorology and Climatology*, 52, 1779–1802. <https://doi.org/10.1175/JAMC-D-12-0256.1>
- Klein, P., Bonin, T. A., Newman, J. F., Turner, D. D., Chilson, P. B., Wainwright, C. E., et al. (2015). LABLE: A multi-institutional, student-led, atmospheric boundary layer experiment. *Bulletin of the American Meteorological Society*, 96(10), 1743–1764. <https://doi.org/10.1175/BAMS-D-13-00267.1>
- Klein, P. M., Hu, X. M., Shapiro, A., & Xue, M. (2016). Linkages between boundary-layer structure and the development of nocturnal low-level jets in central Oklahoma. *Boundary-Layer Meteorology*, 158(3), 383–408. <https://doi.org/10.1007/s10546-015-0097-6>
- Klein, P. M., Hu, X. M., & Xue, M. (2014). Impacts of mixing processes in nocturnal atmospheric boundary layer on urban ozone concentrations. *Boundary-Layer Meteorology*, 150(1), 107–130. <https://doi.org/10.1007/s10546-013-9864-4>
- Lundquist, J. K., & Mirocha, J. D. (2008). Interaction of nocturnal low-level jets with urban geometries as seen in joint urban 2003 data. *Journal of Applied Meteorology and Climatology*, 47(1), 44–58. <https://doi.org/10.1175/2007JAMC1581.1>
- Mao, H., & Talbot, R. (2004). Role of meteorological processes in two New England ozone episodes during summer 2001. *Journal of Geophysical Research*, 109, D20305. <https://doi.org/10.1029/2004JD004850>
- Ohya, Y., Nakamura, R., & Uchida, T. (2008). Intermittent bursting of turbulence in a stable boundary layer with low-level jet. *Boundary-Layer Meteorology*, 126(3), 349–363. <https://doi.org/10.1007/s10546-007-9245-y>
- Ostdiek, V., & Blumen, W. (1997). A dynamic trio: Inertial oscillation, deformation frontogenesis and the Ekman-Taylor boundary layer. *Journal of the Atmospheric Sciences*, 54(11), 1490–1502. [https://doi.org/10.1175/1520-0469\(1997\)054<1490:ADTIOD>2.0.CO;2](https://doi.org/10.1175/1520-0469(1997)054<1490:ADTIOD>2.0.CO;2)
- Parish, T. R. (2016). A comparative study of the 3 June 2015 Great Plains low-level jet. *Monthly Weather Review*, 144(8), 2963–2979. <https://doi.org/10.1175/MWR-D-16-0071.1>
- Parish, T. R., & Clark, R. D. (2017). On the initiation of the 20 June 2015 Great Plains low-level jet. *Journal of Applied Meteorology and Climatology*, 56(7), 1883–1895. <https://doi.org/10.1175/JAMC-D-16-0187.1>
- Reif, D. W., & Bluestein, H. B. (2017). A 20-year climatology of nocturnal convection initiation over the central and Southern Great Plains during the warm season. *Monthly Weather Review*, 145(5), 1615–1639. <https://doi.org/10.1175/MWR-D-16-0340.1>
- Rife, D. L., Pinto, J. O., Monaghan, A. J., Davis, C. A., & Hannan, J. R. (2010). Global distribution and characteristics of diurnally varying low-level jets. *Journal of Climate*, 23(19), 5041–5064. <https://doi.org/10.1175/2010JCLI3514.1>
- Shapiro, A., Fedorovich, E., & Rahimi, S. (2016). A unified theory for the Great Plains nocturnal low-level jet. *Journal of the Atmospheric Sciences*, 73(8), 3037–3057. <https://doi.org/10.1175/JAS-D-15-0307.1>
- Shapiro, A., Fedorovich, E., & Gebauer, J. G. (2018). Mesoscale ascent in nocturnal low-level jets. *Journal of the Atmospheric Sciences*, 75(5), 1403–1427. <https://doi.org/10.1175/jas-d-17-0279.1>
- Smith, E. N., Gebauer, J. G., Klein, P. M., Fedorovich, E., & Gibbs, J. A. (2019). The Great Plains low-level jet during PECAN: Observed and simulated characteristics. *Monthly Weather Review*, 147(6), 1845–1869. <https://doi.org/10.1175/mwr-d-18-0293.1>
- Song, J., Liao, K., Coulter, R. L., & Lesht, B. M. (2005). Climatology of the low-level jet at the Southern Great Plains atmospheric boundary layer experiments site. *Journal of Applied Meteorology*, 44(10), 1593–1606. <https://doi.org/10.1175/JAM2294.1>
- Stelten, S., & Gallus, W. A. (2017). Pristine nocturnal convective initiation: A climatology and preliminary examination of predictability. *Weather and Forecasting*, 32(4), 1613–1635. <https://doi.org/10.1175/WAF-D-16-0222.1>
- Stensrud, D. J. (1996). Importance of low-level jets to climate: A review. *Journal of Climate*, 9(8), 1698–1711. [https://doi.org/10.1175/1520-0442\(1996\)009<1698:IOLJLT>2.0.CO;2](https://doi.org/10.1175/1520-0442(1996)009<1698:IOLJLT>2.0.CO;2)
- Sun, J., Mahrt, L., Banta, R. M., & Pichugina, Y. L. (2012). Turbulence regimes and turbulence intermittency in the stable boundary layer during CASES-99. *Journal of the Atmospheric Sciences*, 69(1), 338–351. <https://doi.org/10.1175/JAS-D-11-082.1>
- Trier, S. B., Wilson, J. W., Ahijevych, D. A., & Sobash, R. A. (2017). Mesoscale vertical motions near nocturnal convection initiation in PECAN. *Monthly Weather Review*, 145(8), 2919–2941. <https://doi.org/10.1175/MWR-D-17-0005.1>
- Van de Wiel, B. J. H., Moene, A. F., Jonker, H. J. J., Baas, P., Basu, S., Donda, J. M. M., et al. (2012). The minimum wind speed for sustainable turbulence in the nocturnal boundary layer. *Journal of the Atmospheric Sciences*, 69(11), 3116–3127. <https://doi.org/10.1175/JAS-D-12-0107.1>
- Vanderwende, B. J., Lundquist, J. K., Rhodes, M. E., Takle, E. S., & Irvin, S. L. (2015). Observing and simulating the summertime low-level jet in central Iowa. *Monthly Weather Review*, 143(6), 2319–2336. <https://doi.org/10.1175/MWR-D-14-00325.1>
- Walters, C. K., Winkler, J. A., Husseini, S., Keeling, R., Nikolic, J., & Zhong, S. (2014). Low-level jets in the North American Regional Reanalysis (NARR): A comparison with rawinsonde observations. *Journal of Applied Meteorology and Climatology*, 53(9), 2093–2113. <https://doi.org/10.1175/JAMC-D-13-0364.1>

- Walters, C. K., Winkler, J. A., Shadbolt, R. P., van Ravensway, J., & Bierly, G. D. (2008). A long-term climatology of southerly and northerly low-level jets for the Central United States. *Annals of the Association of American Geographers*, 98(3), 521–552. <https://doi.org/10.1080/00045600802046387>
- Wang, Y., Klipp, C. L., Garvey, D. M., Ligon, D. A., Williamson, C. C., Chang, S. S., et al. (2007). Nocturnal low-level-jet-dominated atmospheric boundary layer observed by a Doppler lidar over Oklahoma City during JU2003. *Journal of Applied Meteorology and Climatology*, 46(12), 2098–2109. <https://doi.org/10.1175/2006JAMC1283.1>
- Whiteman, C. D., Bian, X., & Zhong, S. (1997). Low-level jet climatology from enhanced rawinsonde observations at a site in the Southern Great Plains. *Journal of Applied Meteorology*, 36(10), 1363–1376. [https://doi.org/10.1175/1520-0450\(1997\)036<1363:LLJCFE>2.0.CO;2](https://doi.org/10.1175/1520-0450(1997)036<1363:LLJCFE>2.0.CO;2)
- Wu, Y., & Raman, S. (1998). The summertime Great Plains low level jet and the effect of its origin on moisture transport. *Boundary-Layer Meteorology*, 88(3), 445–466. <https://doi.org/10.1023/A:1001518302649>